Experimental Research on Mineralogical Characteristics and Mechanical Properties of Montney Siltstone from Northeastern British Columbia (Part of NTS 092A) Using Indentation Tests and Scanning Electron Microscope–Energy Dispersive Spectrometry Analysis

H. Yu[1], School of Engineering, University of Northern British Columbia, Prince George, British Columbia (yuh0@unbc.ca)

W. Zheng, School of Engineering, University of Northern British Columbia, Prince George, British Columbia

Yu, H. and Zheng, W. (2025): Experimental research on mineralogical characteristics and mechanical properties of Montney siltstone from northeastern British Columbia (part of NTS 092A) using indentation tests and scanning electron microscope–energy dispersive spectrometry analysis; *in* Geoscience BC Summary of Activities 2024, Geoscience BC, Report 2025-01, p. 67–74.

Introduction

Natural gas production from unconventional formations has surged over the past two decades, driven by advancements in horizontal drilling and multistage hydraulic fracturing (Sharma et al., 2019; Cheng et al., 2022). In northeastern British Columbia (BC), the Montney gas play has become the largest gas producer in the province, with two-thirds of drilled wells targeting the siltstone-rich Montney Formation (Rivard et al., 2014; Vishkai et al., 2017). The effectiveness of hydraulic fracturing in creating fracture networks is closely linked to the mechanical properties of the target formations, which are significantly influenced by the mineralogical composition of the rock (Rivard et al., 2014; Cheng et al., 2022). Additionally, localized mechanical properties of the rock affect proppant embedment within fractures, thereby impacting fracture conductivity (Zheng et al., 2019). Thus, understanding the relationship between the mechanical parameters of the rock and its mineralogy at the microscale is critical.

The micro-indentation test was initially developed to determine the hardness and elastic modulus of thin films and small solid samples by measuring indentation depth as a function of increasing force applied by an indenter (Poon et al., 2008). Compared to traditional compression tests, the indenter applies force to a small area, creating high, localized stress that enables the measurement of mechanical properties at the microscale (Kasyap et al., 2021; Song et al., 2022). Meanwhile, scanning electron microscopy (SEM) provides high-resolution micromorphologies of sample surfaces by using a focused high-energy electron beam to excite various physical signals through its interaction with the sample (Fandrich et al., 2007). Additionally, the energy dispersive spectrometry (EDS) system, attached to the SEM, allows for chemical analysis of the scanned area (Meyer et al., 2013;

Five disk-shaped rock samples obtained from cores drilled at depths ranging from 2068.29 to 2337.39 m within the Lower Triassic Montney play in northeastern BC were used in this study. Nine instrumented indentation tests were performed on each sample to generate force-displacement curves, from which the local Young's modulus and hardness at each indentation site were determined. Following the indentation tests, SEM and EDS analyses were conducted to create digital mineral maps, enabling identification of the mineral composition and localized microstructure at the indentation sites. Finally, the influence of the mineralogical composition of the rock on its mechanical properties is discussed.

Materials and Methods

Materials

The five samples were prepared from the drillcore from well TOURMALINE HZ TOWN C-031-H/094-B-09 (well authorization 28232, unique well identifier 200C031H094B0900; BC Energy Regulator, 2024a), located in the Lower Triassic Montney play in northeastern BC, as shown in Figure 1. The measured depths of the cores ranged from 2068.29 to 2337.39 m. For comparison purposes, the cores were selected from two formations: samples S1 (2068.29 m) and S2 (2068.55 m) were taken from the Doig Formation, while samples S3 (2265.85 m), S4 (2336.04 m) and S5 (2336.37 m) were extracted from the Montney Formation.

The samples were obtained by drilling horizontally into cores (Figure 2a) and then trimmed into disk shapes with a nominal diameter of 25.4 mm. The lateral surfaces of the samples were coated with an epoxy resin (Figure 2b). To minimize the effects of surface roughness on the indentation tests, the flat surfaces were polished using a Buehler

[1] *The lead author is a 2024 Geoscience BC Scholarship recipient.*

This publication is also available, free of charge, as colour digital files in Adobe Acrobat® PDF format from the Geoscience BC website: https://geosciencebc.com/updates/summary-of-activities/.

Figure 1. Location of the Montney unconventional gas play (modified from BC Energy Regulator, 2024b). The Montney play area and other oil and gas resource basins, including the Liard and Horn River basins, and Cordova Embayment are shown; the yellow star indicates the location of the sampled well.

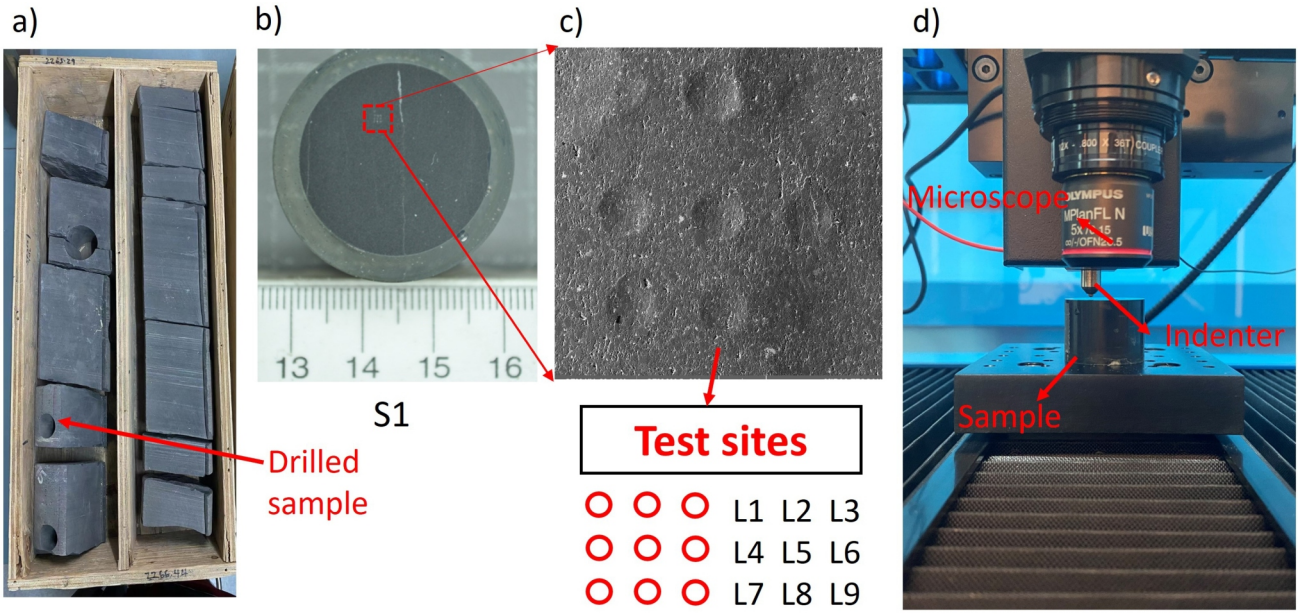

Figure 2. Instrumented indentation test performed on samples from the Montney play: **a)** drillcore from well sampled at approximately 2068 m (red arrow indicates the location and orientation of the sample plug extracted); **b)** sample plug S1 (diameter of 25.4 mm); **c)** nine test sites, labelled L1–L9, for the Brinell hardness testing indenter arranged in a three-by-three grid (red polygon in panel b shows test site location); **d)** Nanovea-M1™ instrumented indentation machine.

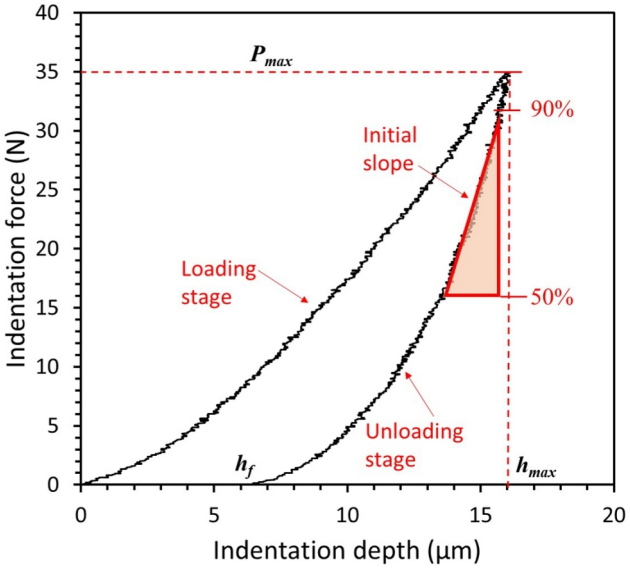

Figure 3. Typical force-displacement curve for instrumented indentation test results from test site L5 of drilled sample S1 from the Montney play. The force-displacement curve is divided into two segments: the loading and unloading stages. The range of 90 to 50% of the maximum force (P_{max}) for the unloading-stage curve is selected and fitted versus indentation depth (h) using a power-law function. The initial slope of this fitted curve represents the contact stiffness, as illustrated by the triangle in the figure. Abbreviations: f, full; max, maximum; N, newton; m, micrometre.

AutoMet® 250 Pro grinder-polisher; surface roughness was also scanned using a profiler, yielding values less than 0.4 µm.

Experimental Method

Instrumented Indentation Test

The Nanovea-M1™ instrumented indentation machine (Figure 2d) was used to perform the instrumented indentation test, employing a Brinell hardness testing indenter—a spherical tungsten carbide ball with a 1 mm diameter. Each sample had nine test locations, labelled L1 to L9, arranged in a three-by-three grid, as shown in Figure 2c. During the test, the indentation force increased at the loading stage to a maximum of 35 newtons (N), then decreased to 0 N at the unloading stage. A constant rate of 17.5 N/min was applied for both the loading and unloading stages. The typical force-displacement curve is presented in Figure 3.

Notably, the final indentation depth did not fully recover to 0 after unloading. This remaining depth is known as the plastic depth, whereas the difference between the maximum and final depths is referred to as the elastic depth. The unloading curve can thus be used to calculate local mechanical properties, such as Young's modulus and hardness. This method assumes that the recoverable depth represents only elastic deformation during unloading (Oliver and Pharr, 2004) and the unloading curve of indentation force (P) versus indentation depth (h) is used for this calculation.

The P-h curve is a fitting power-law equation:

$$P \quad (h \quad h_f)^m$$

where α, m and h_f are fitting constants.

S is the contact stiffness, which is determined by the initial slope (90–50%) of the P-h curve:

$$S \quad m \ (h \quad h_f)^{m \ 1}$$

The contacted depth (h_c) between the indenter and sample can be calculated as:

$$h_c \quad h_{\max} \quad P_{\max} / S$$

where $h_{\max}$ is maximum depth, $P_{\max}$ is maximum force, and is the constant depending on the geometry of the indenter; for the Brinell hardness testing indenter, it is 0.75. Based on the h_c, the contact projected area (A_c) between the Brinell indenter and sample can be calculated as:

$$A_c \quad (r^2 \quad [r^2 \quad h_c]^2)$$

where r is the radius of the spherical indenter (0.5 mm). When A_c is determined, the indentation hardness (H) can be obtained as:

$$H \quad P_{\max} / A_c$$

The efficient Young's modulus (E_{eff}) presents the apparent Young's modulus between sample and indenter, which is calculated as:

$$E_{eff} \quad \sqrt{\ } s / 2 \sqrt{A_c}$$

where β is the effective coefficient of all physical processes, which is 1.05 in this study.

Moreover, Young's modulus (E) of the sample is calculated as:

$$E \quad (1 \quad v^2) / (\frac{1}{E_{eff}} \quad \frac{1 \quad v_i^2}{E_i})$$

where v and E are the Poisson's ratio and Young's modulus of the sample, respectively, and v_i and E_i are the Poisson's ratio and Young's modulus of the indenter. In this study, v_i equals 0.31 and E_i equals 600 GPa are used for the tungsten carbide Brinell indenter, and v equals 0.30 is used for the rock sample.

SEM and EDS Analysis

Scanning electron microscopy (SEM) and energy dispersive spectrometry (EDS) analyses were performed on indents from test sites L1 to L9 following the completion of the indentation tests. The electron images of SEM and elemental distributions from EDS were obtained using a Tescan Mira3 XMU scanning electron microscope equip-

ped with a field emission gun and a X-Max Energy Dispersive Spectrometer detector made by Oxford Instruments. Typical SEM and EDS images are presented in Figure 4. The high-resolution SEM images revealed anisotropic micromorphological features of the localized rock (Figure 4a), whereas the EDS images, shown in different colours, displayed the distributions of chemical elements corresponding to various mineral types (Figure 4b–i).

The online library of the BC Energy Regulator (previously BC Oil and Gas Commission) houses a digital archive of well data and reports available to the public. The X-ray diffraction (XRD) data for rock samples from the same study well and at similar depths were retrieved from this archive to inform this research (Mineralogy, Inc., 2014). Consequently, the mineral composition of the samples at each depth was determined. Using the chemical formulas of known minerals, the chemical elements identified in the layered EDS images were used to determine local mineral types at the same locations. For example, quartz (SiO_2) contains only Si and O; pyrite (FeS_2) contains only Fe and S; muscovite $\{KAl_2(Si_3AlO_{10})(OH)_2\}$ was determined by the presence of Si, Al and K; and albite ($NaAlSi_3O_8$) was determined by the presence of Si, Al and Na.

Results

Young's Modulus and Hardness

Based on the results of the unloading *P-h* curves from the instrumented indentation tests, Young's modulus and hardness were determined. To ensure precision, the results from some test sites were discarded due to fluctuations in the instrumented indentation tests and the failure of EDS analysis to detect certain elements. Table 1 presents the average, standard deviation, and coefficient of variation for Young's modulus and hardness for each sample. The results show

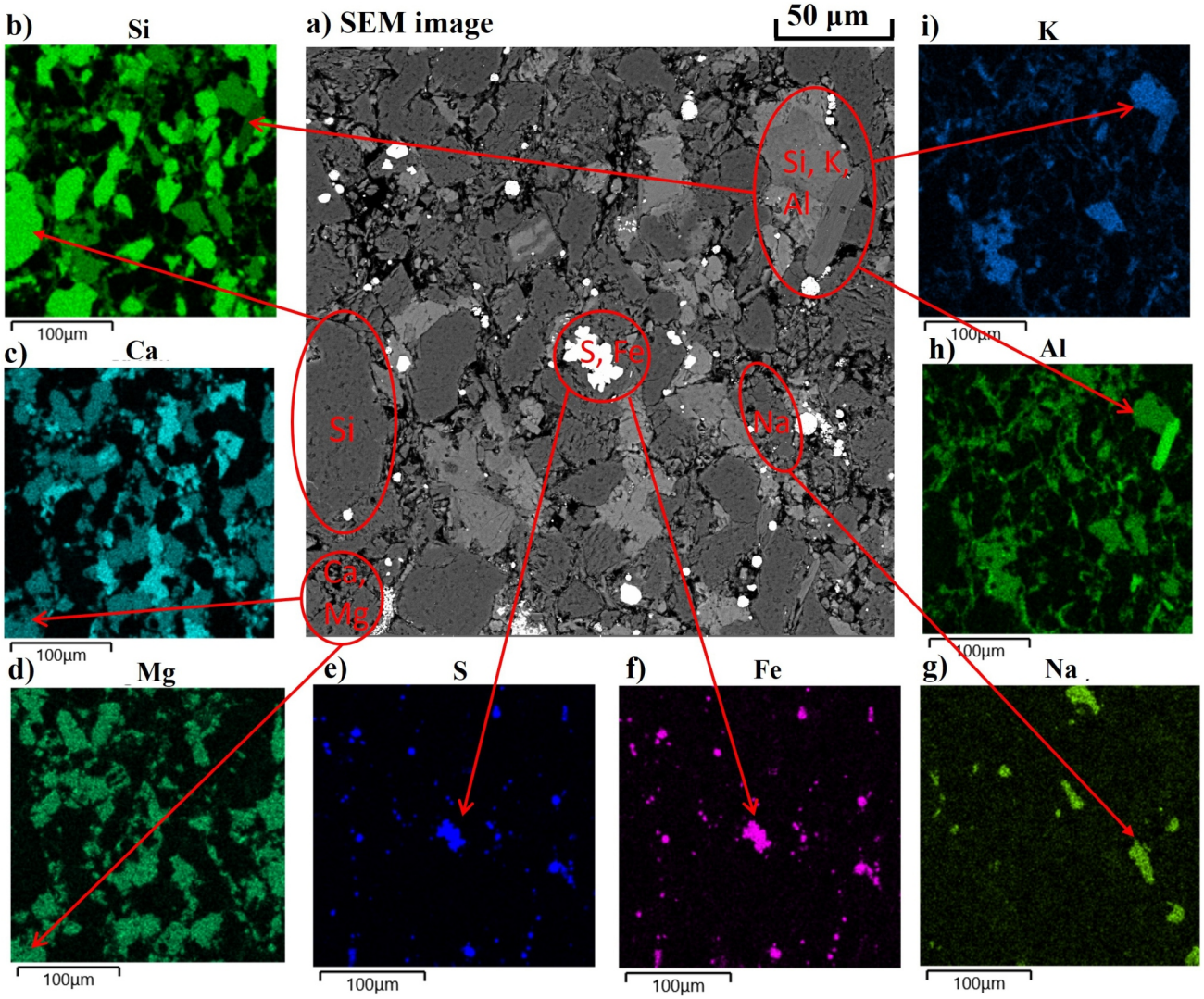

Figure 4. Typical scanning electron microscopy (SEM) image of **a)** test site L1 of sample S1 from the Montney play and energy dispersive spectrometry (EDS) elemental maps of **b)** silicon (Si); **c)** calcium (Ca); **d)** magnesium (Mg); **e)** sulphur (S); **f)** iron (Fe); **g)** sodium (Na); **h)** aluminium (Al); **i)** potassium (K).

that samples from similar depths exhibit comparable values for Young's modulus and hardness. Additionally, mechanical properties vary between samples from different depths within the Montney Formation. Test locations at the shallower depth (S3 at approximately 2265 m) show a lower average Young's modulus compared to those at greater depths (S4 and S5 at approximately 2336 m). The average values of Young's modulus of the Doig Formation samples (S1 and S2) are higher than that of the Montney Formation at around 2265 m (S3), but lower than those at around 2336 m (S4 and S5). For hardness, S2 from the Doig Formation exhibits the highest average value (0.94 GPa), whereas S5 from the Montney Formation has the lowest (0.69 GPa).

Figure 5 presents the scatter plot of Young's modulus and hardness for all samples at various depths. Due to the similarity in mechanical properties among samples from similar depths, the scatter plot illustrates three distinct groups corresponding to the three depth levels. The red dots represent samples from the Doig Formation at approximately 2068 m (S1 and S2), whereas the blue triangles at 2265 m (S3) and the black squares at 2336 m (S4 and S5) correspond to samples from the Montney Formation. The dashed lines in Figure 5 represent the linear fit between Young's modulus and hardness for the three groups. Results indicate significant correlation between Young's modulus and hardness for samples from similar depths within the same formation, with R^2 values of 0.98, 0.97 and 0.98. Additionally, the coefficient (y) of the fitting equation reflects the ratio between Young's modulus and hardness. For the Montney Formation, the sample from 2265 m (S3) exhibits a lower linear coefficient (23.14) compared to samples from 2336 m (S4 and S5) with a higher linear coefficient (71.07). In contrast, the linear coefficient (40.61) of Doig Formation samples (S1 and S2) is larger than that of S3 at 2265 m but smaller than that of S4 and S5 at 2336 m.

Mineral Composition and Microstructure

Digital mineral maps were generated from EDS images of chemical elements using in-house MATLAB® code. A typical mineral map for samples from different depths is shown in Figure 6a. According to the map, samples from various depths exhibit differences in mineral grain sizes and com-

Table 1. Average (Avg), standard deviation (std) and coefficient of variation (Cv) of Young's modulus and hardness for the five samples (S1–S5) from the Montney play.

Specimen number	Dataset count	Depth (m)	Young's modulus (GPa)		Hardness (GPa)	
			Avg ±std	Cv	Avg ±std	Cv
S1	5	2068.29	32.62 ±15.35	0.44	0.81 ±0.14	0.17
S2	9	2068.55	36.80 ±2.23	0.06	0.94 ±0.06	0.07
S3	8	2265.85	20.14 ±3.38	0.17	0.87 ±0.10	0.12
S4	7	2336.04	63.34 ±3.66	0.06	0.83 ±0.03	0.04
S5	6	2336.37	42.75 ±4.41	0.1	0.69 ±0.13	0.19

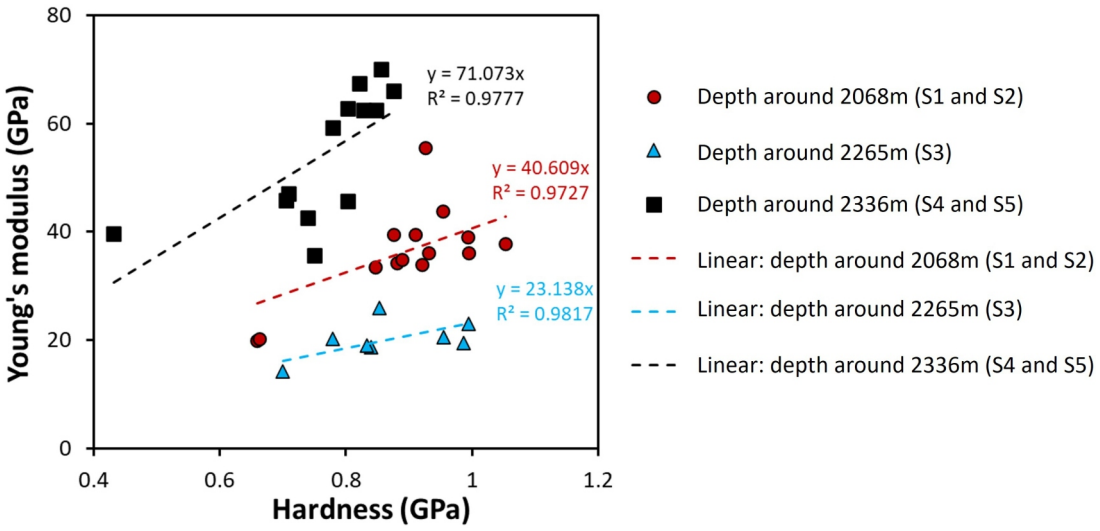

Figure 5. Young's modulus versus hardness for samples from different depths in the Montney play: circles, dashed line and values in red represent indentation results and fitting result of samples S1 and S2 from the Doig Formation at approximately 2068 m; triangles, dashed line and values in blue represent indentation results and fitting result of sample S3 from the Montney Formation at approximately 2265 m; squares, dashed line and values in black represent indentation results and fitting result of samples S4 and S5 from the Montney Formation at approximately 2336 m. Abbreviation: GPa, gigapascal.

positions. The mineral grain sizes of samples from approximately 2068 m in the Doig Formation range from 20 to 50 µm, with the primary load-bearing framework composed of coarse minerals, including calcite, dolomite, albite and quartz. Samples from around 2265 m in the Montney Formation have grain sizes between 10 and 50 µm. The carbonate mineral (calcite and dolomite) content in samples from 2265 m is of smaller grain size than that of samples from 2068 m. Samples from 2336 m in the Montney Formation have grain sizes of less than 20 µm where clay minerals form the rock matrix, with harder minerals embedded within the clay.

The average area percentages (A%) of pores and minerals for each sample, including all indentation locations, were measured from the digital mineral maps and the results are presented in Figure 6b. Quartz had the highest average area percentage across all samples, whereas albite, pyrite and chlorite had the lowest values. Small amounts of titanium dioxide (TiO_2) were also identified in samples S3, S4 and S5. The average area percentage of carbonate minerals was relatively high in samples S1 and S2, whereas clay minerals (muscovite and chlorite) had a higher average area percentage in samples S4 and S5 than carbonate minerals. Sample S3 exhibited a relatively balanced distribution of carbonate and clay minerals. Table 2 presents the average, standard deviation and coefficient of variation for the area percentage of pores and each mineral across all test sites. The results show a very low coefficient of variation of only 0.25 for quartz, whereas it is very large (1.2) for titanium dioxide; however, the average area percentage is very small and titanium dioxide is found only in samples S3, S4 and S5.

Discussion

Impacts of Mineral Types on Mechanical Properties

The Pearson correlation coefficient was used to assess the impact of mineral content on Young's modulus and hardness. The p-values for the Pearson correlation range from 0 to 1, with a p-value less than 0.05 indicating a statistically significant correlation between the two variables. The correlation coefficient (R) ranges from –1 to 1, where a negative R indicates a negative correlation and a positive R indicates a positive correlation. Note that results from test sites due to fluctuations in the instrumented indentation test were discarded, as were those from EDS analyses in which elements had been missed. Figure 7 presents scatter plots of mineral average area percentage (A%) versus hardness and Young's modulus, along with the corresponding correlation coefficients. In these plots, the horizontal axis represents the average area percentage of each mineral, whereas the vertical axis indicates hardness and Young's modulus.

Based on the p-values and R coefficient, calcite (P = 0.048, R = 0.337) shows a positive correlation with hardness. Meanwhile, a positive relationship is observed between dolomite and hardness (P = 0.057, R = 0.325), although its p-value is slightly above 0.05. This finding aligns with the conclusions presented earlier in this paper, where S2 exhib-

Table 2. Average (Avg), standard deviation (Std) and coefficient of variation (Cv) for the area percentage of pores and each mineral across all test sites in the Montney play.

	Area percentage (%)									
	Porosity	Albite	Calcite	Dolomite	Muscovite	Orthoclase	Pyrite	Chlorite	Titanium dioxide	Quartz
Avg	2.75	6.91	13.75	15.39	14.25	8.67	1.68	2.47	0.12	34.01
Std	2.43	3.98	6.71	11.47	7.64	4.02	0.87	2.39	0.14	8.47
Cv	0.89	0.58	0.49	0.75	0.54	0.46	0.52	0.97	1.20	0.25

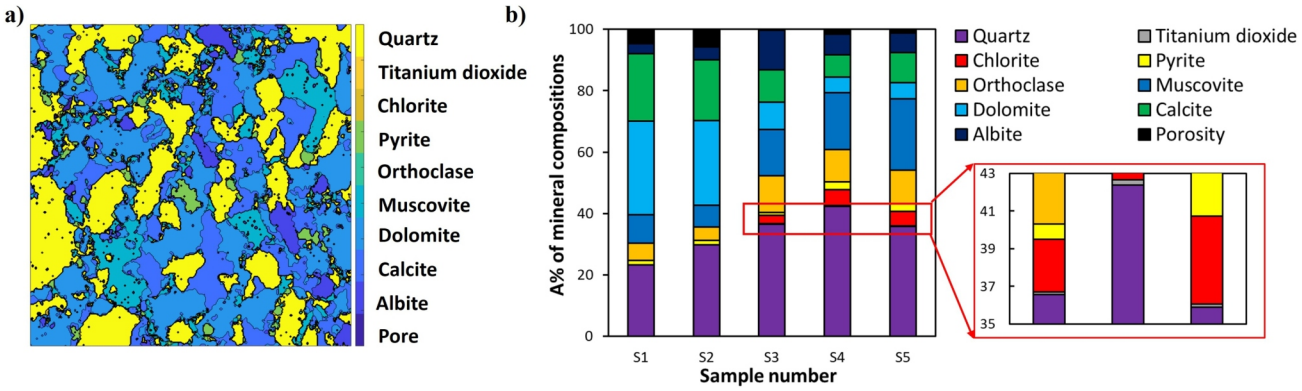

Figure 6. Mineral map and average area percentage of minerals for samples from the Montney play: **a)** typical digital mineral map for test site L1 of sample S1, with colours representing different minerals and the scale bar indicating mineral types; **b)** average area percentage (A%) of pores and minerals for each sample, with close-up (red box) showing the locations of small amounts of titanium dioxide.

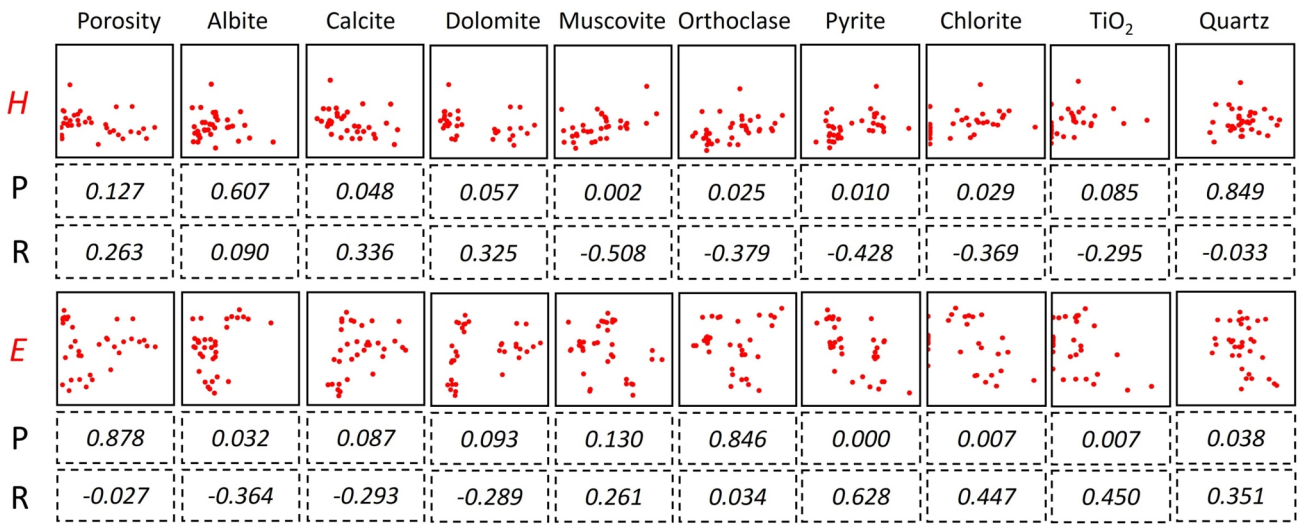

Figure 7. Scatter plots of indentation depth versus mineral area percentage (A%) and porosity for samples from the Montney play, with Pearson correlation coefficient (R) and p-value (P): red scatter plots show the relationships of hardness (*H*) and Young's modulus (*E*) with A%. For plots in the same row, the vertical axis is consistently scaled, whereas the horizontal axis varies according to the A% of the minerals. These plots visually demonstrate the relationships between different minerals and Young's modulus and hardness. The p-value indicates whether a significant linear relationship exists, whereas the R coefficient reflects the strength of this relationship. Abbreviation: TiO_2, titanium dioxide.

its the greatest hardness with the higher average area percentage of calcite and dolomite (Figure 6b), whereas orthoclase (P = 0.025, R = –0.379), pyrite (P = 0.010, R = –0.428), muscovite (P = 0.002, R = –0.508) and chlorite (P = 0.029, R = –0.369) exhibit negative correlations with hardness. Similarly, S5 has the highest average area percentage of muscovite and orthoclase (Figure 6b) and exhibits the lowest hardness. In addition, pyrite (P = 0.000, R = 0.628), chlorite (P = 0.007, R = 0.447) and titanium dioxide (TiO_2; P = 0.007, R = 0.450) exhibit positive correlations with Young's modulus, whereas albite (P = 0.032, R = –0.364) is negatively correlated with Young's modulus. This further corroborates the earlier result shown in Figure 5, where sample S3, with the highest albite content, exhibits the lowest Young's modulus.

These findings indicate a correlation between the mechanical properties of the rock and its mineral composition. An increase in carbonate minerals (calcite and dolomite) enhances rock hardness. Conversely, an increase in clay mineral content (muscovite and chlorite) decreases hardness but increases Young's modulus, whereas higher albite content reduces Young's modulus. However, in this study, the lack of observed correlations between porosity and other minerals, such as quartz, may be due to the limited variation in quartz content, as evidenced by a coefficient of variation of only 0.25 for quartz (Table 2). Therefore, it cannot be concluded that these factors have no impact on the mechanical properties of the rock.

Conclusion

Instrumented indentation tests and scanning electron microscope–energy dispersive spectrometry analyses were conducted on five samples from the Montney unconventional gas play in British Columbia. The indentation tests measured local Young's modulus and hardness, whereas mineral compositions were identified through scanning electron microscope–energy dispersive spectrometry analysis. The key findings of the study are summarized as follows:

1) Images of chemical elements obtained through scanning electron microscope–energy dispersive spectrometry analysis facilitate their identification in different regions, enabling the construction of a localized mineral map. According to the mineral map, the grain size of minerals decreases with depth in the sampled well, with the Doig Formation characterized by the presence of more carbonate minerals than the Montney Formation, which contains more clay minerals.

2) Samples from similar depths exhibit comparable mechanical properties, with Young's modulus and hardness showing a linear correlation. For the ratio of Young's modulus to hardness, samples from the Montney Formation at 2336 m show the highest values, that from the Montney Formation at 2265 m the lowest, whereas the samples from the Doig Formation at 2068 m exhibit intermediate values.

3) A correlation is observed between the mechanical properties of the rock and mineral composition: an increase in carbonate minerals (calcite and dolomite) enhances hardness, whereas higher clay mineral content (muscovite and chlorite) reduces hardness but increases Young's modulus. Additionally, increased albite content is associated with a lower Young's modulus.

The findings highlight the influence of mineral composition on the localized mechanical properties of rock formations, revealing the effects of carbonate and clay minerals on rock behaviour. Future work will include a broader set of experimental samples to investigate the impact of minerals with limited variability in this study, with the aim of developing a predictive model from which rock properties based on mineral composition can be derived.

Acknowledgments

The authors gratefully acknowledge the financial support from Geoscience BC through the Geoscience BC Scholarship program, which was essential to the progress of this study. Additional support was provided by the Natural Sciences and Engineering Research Council of Canada (NSERC) and the University of Northern British Columbia (UNBC). The authors also thank C. Kang for offering valuable feedback during the peer review process.

References

and Artuner, H. (2015): Application of Decision Tree Algorithm for classification and identification of natural minerals using SEM–EDS; Computers & Geosciences, v. 80, p. 38–48, URL <https://doi.org/10.1016/j.cageo.2015.03.015>.

BC Energy Regulator (2024a): Well lookup and reports; BC Energy Regulator, URL <https://www.bc-er.ca/data-reports/data-centre/> [November 2024].

BC Energy Regulator (2024b): British Columbia's 2023 oil and gas reserves and production report; BC Energy Regulator, URL <https://www.bc-er.ca/files/reports/Reserves-and-Production-Reports/2023-Oil-and-Gas-Reserves-and-Production-Report.pdf> [October 2024].

Cheng, P., Zhang, C.P., Ma, Z.Y., Zhou, J.P., Zhang, D.C., Liu, X.F., Chen, H. and Ranjith, P.G. (2022): Experimental study of micromechanical properties alterations of shale matrix treated by $ScCO_2$-Water saturation using nanoindentation tests; Energy, v. 242, art. 122965, URL <https://doi.org/10.1016/j.energy.2021.122965>.

Fandrich, R., Gu, Y., Burrows, D. and Moeller, K. (2007): Modern SEM-based mineral liberation analysis; International Journal of Mineral Processing, v. 84, no. 1–4, p. 310–320, URL <https://doi.org/10.1016/j.minpro.2006.07.018>.

Kasyap, S.S., Li, S. and Senetakis, K. (2021): Investigation of the mechanical properties and the influence of micro-structural characteristics of aggregates using micro-indentation and Weibull analysis; Construction and Building Materials, v. 271, art.121509, URL <https://doi.org/10.1016/j.conbuildmat.2020.121509>.

Meyer, M.C., Austin, P. and Tropper, P. (2013): Quantitative evaluation of mineral grains using automated SEM–EDS analysis and its application potential in optically stimulated luminescence dating; Radiation Measurements, v. 58, p. 1–11, URL <https://doi.org/10.1016/j.radmeas.2013.07.004>.

Mineralogy, Inc. (2014): Final test report–X-ray diffraction analysis: well C-031-H/094-B-09; prepared for Shell Canada Limited, submitted to BC Oil and Gas Commission, URL <https://files.bc-er.ca/> [October 2024].

Oliver, W.C. and Pharr, G.M. (2004): Measurement of hardness and elastic modulus by instrumented indentation: advances in understanding and refinements to methodology; Journal of Materials Research, v. 19, p. 3–20, URL <https://doi.org/10.1557/jmr.2004.19.1.3>.

Poon, B., Rittel, D. and Ravichandran, G. (2008): An analysis of nanoindentation in linearly elastic solids; International Journal of Solids and Structures, v. 45, no. 24, p. 6018–6033, URL <https://doi.org/10.1016/j.ijsolstr.2008.07.021>.

Rivard, C., Lavoie, D., Lefebvre, R., Séjourné, S., Lamontagne, C. and Duchesne, M. (2014): An overview of Canadian shale gas production and environmental concerns; International Journal of Coal Geology, v. 126, p. 64–76, URL <https://doi.org/10.1016/j.coal.2013.12.004>.

Sharma, P., Prakash, R. and Abedi, S. (2019): Effect of temperature on nano- and microscale creep properties of organic-rich shales; Journal of Petroleum Science and Engineering, v. 175, p. 375–388, URL <https://doi.org/10.1016/j.petrol.2018.12.039>.

Song, J., Xiang, D., Hu, D., Zhou, H., Guo, D. and Zhang, G. (2022): Creep characteristics of a fracturing fluid-softened shale investigated by microindentation; International Journal of Rock Mechanics and Mining Sciences, v. 152, art. 105067, URL <https://doi.org/10.1016/j.ijrmms.2022.105067>.

Vishkai, M., Wang, J., Wong, R.C.K., Clarkson, C.R. and Gates, I.D. (2017): Modeling geomechanical properties in the Montney formation, Alberta, Canada; International Journal of Rock Mechanics and Mining Sciences, v. 96, p. 94–105, URL <https://doi.org/10.1016/j.ijrmms.2017.04.001>.

Zheng, W., Tannant, D.D., Cui, X., Xu, C. and Hu, X. (2019): Improved discrete element modeling for proppant embedment into rock surfaces; Acta Geotechnica, v. 15, no. 2, p. 347–364, URL <https://doi.org/10.1007/s11440-019-00819-5>.